

# Fault Zone Imaging with Distributed Acoustic Sensing: Body-to-Surface Wave Scattering

James Atterholt<sup>1</sup>, Zhongwen Zhan<sup>1</sup>, Yan Yang<sup>1</sup>

<sup>1</sup>Seismological Laboratory, California Institute of Technology, Pasadena, California, USA 91125

## Key Points:

- We develop a framework for systematically locating fault zones at sub-kilometer scales using the DAS-measured earthquake wavefield.
- We present a model for these fault zones and use simulations to show that this model reproduces first-order observations of scattering.
- By comparing observations with synthetics, we use this method to constrain local fault zone geometry.

---

Corresponding author: James Atterholt, [atterholt@caltech.edu](mailto:atterholt@caltech.edu)

**Abstract**

Fault zone structures at many scales largely dictate earthquake ruptures and are controlled by the geologic setting and slip history. Characterizations of these structures at diverse scales inform better understandings of earthquake hazards and earthquake phenomenology. However, characterizing fault zones at sub-kilometer scales has historically been challenging, and these challenges are exacerbated in urban areas, where locating and characterizing faults is critical for hazard assessment. We present a new procedure for characterizing fault zones at sub-kilometer scales using distributed acoustic sensing (DAS). This technique involves the backprojection of the DAS-measured scattered wavefield generated by natural earthquakes. This framework provides a measure of the strength of scattering along a DAS array and thus constrains the positions and properties of local scatterers. The high spatial sampling of DAS arrays makes possible the resolution of these scatterers at the scale of tens of meters over distances of kilometers. We test this methodology using a DAS array in Ridgecrest, CA which recorded much of the 2019  $M_w 7.1$  Ridgecrest earthquake aftershock sequence. We show that peaks in scattering along the DAS array are spatially correlated with mapped faults in the region and that the strength of scattering is frequency-dependent. We present a model of these scatterers as shallow, low-velocity zones that is consistent with how we may expect faults to perturb the local velocity structure. We show that the fault zone geometry can be constrained by comparing our observations with synthetic tests.

**Plain Language Summary**

Fault zones are multi-scale structures that govern where and how earthquakes happen. Characterizing fault zones at all scales is thus important for understanding earthquake ruptures and earthquake-related hazards. However, finding and describing fault zones at small scales remains a persistent challenge in earthquake science. We propose a framework for the characterization of fault zones using distributed acoustic sensing (DAS), a recently developed technique that converts fiber optic cables into dense networks of ground motion sensors. Earthquake waves are scattered when they encounter fault zones, and this scattering creates signatures in DAS data that we can use to locate these fault zones. Additionally, the behavior of fault zone scattered waves with frequency may illuminate detailed characteristics of the fault zone. We test this framework using a DAS network in Ridgecrest, CA that recorded aftershocks of the 2019 magnitude 7.1 Ridgecrest earthquake. We use these recordings to map fault zone locations near the network. These locations are close to previously mapped faults but are more accurate. By comparing the behavior of observed fault zone scattered waves with frequency with that of simulations, we can constrain shallow fault zone geometry.

## 1 Introduction

The Earth's crust is a geologically heterogeneous medium that hosts myriad sharp material contrasts at multiple scales. Among these heterogeneities are fault zones, features consisting of fault cores and surrounding zones of fracture that accommodate strain. Finding new ways to locate and characterize fault zones may potentially serve a variety of societally and scientifically important functions. Proximity to fault zones increases the likelihood of severe damage to infrastructure, both because fault zones host static deformation, and because fault zones may amplify ground motion (Kurzon et al., 2014). Additionally, the locations of faults control estimates of fault connectivity, which is an important parameter in some probabilistic hazard estimates (Field et al., 2014). Relatedly, relative fault positioning and fault geometry play a pivotal role in the propagation and termination of earthquakes (Harris & Day, 1993, 1999; Wesnousky, 2008). Fault damage zone scaling is expected to play an influential role in earthquake nucleation (Ampuero et al., 2002), earthquake potency (Weng et al., 2016), and long-term earthquake sequence behavior (Thakur et al., 2020). Importantly, fault zones are multi-scale structures (Faulkner et al., 2010), and thus developing a more complete picture of fault zone structure at sub-kilometer scales contributes to these efforts to evaluate earthquake hazard and geological controls on earthquake phenomenology.

Considerable attention is given to major fault zones, those that are large and accommodate significant strain. But, minor and unmapped fault zones are an important consideration when evaluating the structural deformation and earthquake hazards in a region. Plate deformation is usually not accommodated by a single fault zone, but rather by a broad distribution of fault zones that extend sometimes hundreds of kilometers from the plate boundary, and minor fault zones play a key role in the accommodation of this strain (Scholtz, 2019). In the absence of high deformation rates, minor fault zones can develop a high risk potential if strain accumulates over a long time period, the stress state changes (Freed & Lin, 2001), or the stability of the fault is perturbed (Ellsworth, 2013). Relatedly, many significant earthquakes rupture within minor or unmapped fault zones. For example, the 2019 Ridgecrest earthquake sequence, which included the largest earthquake to take place in California in over two decades, ruptured mostly unmapped faults in the Little Lake and Airport Lake fault zones (Ross et al., 2019), which only accommodated approximately 1 mm/y of slip (Amos et al., 2013).

For both major and minor fault zones, shallow fault zone structure is important. The shallowest few hundred meters of fault zones can exhibit sharp and localized velocity reductions (e.g. Zigone et al., 2019; Y. Wang et al., 2019; Share et al., 2020) that can amplify ground motion, and shallow crustal faults play an important role in both facilitating and impeding the transport of groundwater and hydrocarbons (Bense et al., 2013). Shallow fault zone structure may also be used to infer the contribution of deep fault structure, which is very difficult to constrain, by correcting for shallow structure contributions in depth-integrated fault characterization approaches.

Previous efforts to locate and describe shallow fault zone structures at sub-kilometer scales have typically relied on geologic mapping, seismic surveying, and satellite imagery. Geologic mapping over decades has produced excellent records of Quaternary faults (e.g. USGS & CGS, 2022), but discerning faults using geologic mapping requires careful fieldwork and evidence of faulting at the surface. Seismic surveying produces detailed images of the subsurface, with which fault locations can be inferred (e.g. Liberty et al., 2021; Lay et al., 2021), but surveys are often expensive and logistically challenging, particularly in urban settings. Satellite imagery is also used to map faults, often by identifying topographic anomalies in images (Joyce et al., 2009). More involved processing, such as producing phase gradient maps from InSAR interferograms (Xu et al., 2020), can also be used to identify fractures. These techniques are powerful, but they require surficial evidence of strain that can be imaged from above.

100 Other studies have used the earthquake wavefield to characterize the structure of  
 101 major fault zones. For example, some studies have used fault zone head waves, head waves  
 102 generated by refraction due to a bimaterial contrast across the fault, to image the fault  
 103 interface and constrain the velocity contrast across the fault (e.g. McGuire & Ben-Zion,  
 104 2005; Allam et al., 2014; Share & Ben-Zion, 2018; Qin et al., 2020). Additionally, some  
 105 studies have used travel-time anomalies from regional and teleseismic events to discern  
 106 properties like the width of the damage zone and the velocity reduction within the dam-  
 107 age zone (e.g. Cochran et al., 2009; H. Yang et al., 2020; Qiu et al., 2021; Share et al.,  
 108 2022). Moreover, low velocity structures can amplify ground motion, and some studies  
 109 have used S-wave amplification caused by the reduced velocities in fault damage zones  
 110 to delineate their structure (e.g. Qiu et al., 2021; Song & Yang, 2022). Another approach  
 111 is to use fault zone trapped waves, waves generated by constructive interference of crit-  
 112 ically reflected waves in the fault damage zone, which can be initiated by sources out-  
 113 side the fault zone (Fohrmann et al., 2004) and have been used to constrain the struc-  
 114 ture of fault damage zones (e.g. Ben-Zion et al., 2003; Catchings et al., 2016; Y. Wang  
 115 et al., 2019; Qiu et al., 2021). In general, these techniques are highly effective tools for  
 116 capturing geometric and internal properties of major fault zones. But, fault zones usu-  
 117 ally need to exhibit relatively large and spatially consistent elastic material contrasts for  
 118 these techniques to be used. Hence, these techniques are typically applied to major fault  
 119 zones using targeted deployments of dense networks of sensors. These factors make these  
 120 methods ineffectual for the discovery and characterization of minor fault zones.

121 The weaknesses of these methods motivate the development of complimentary tech-  
 122 niques for identifying and characterizing sub-kilometer scale fractures in the crust. To  
 123 this end, we suggest an alternative method for identifying and characterizing fractures  
 124 in the crust using distributed acoustic sensing (DAS) data. DAS is an emergent tech-  
 125 nology that repurposes fiber optic cables as dense arrays of strainmeters. DAS uses a laser  
 126 interrogator unit to emit pulses of light that probe a fiber optic cable, and natural im-  
 127 perfections in the fiber send echoes back to the interrogator unit. Perturbations of the  
 128 fiber change the travel times of these echoes, and these changes in travel time are quasi-  
 129 linearly proportional to the strain induced by the perturbations. The high spatial fre-  
 130 quency of DAS data allows for the resolution of high wavenumber phenomena that are  
 131 incoherent in more sparsely measured data, which is useful for characterizing fault zones  
 132 at high resolution (Jousset, 2019). One such phenomenon is the scattering of earthquake  
 133 body waves to surface waves due to small-scale, local heterogeneities in the upper crust.  
 134 We show an example of this scattering in Figure 1, and we subsequently refer to these  
 135 features as chevrons, owing to their chevron-like shape in DAS data representations. These  
 136 chevrons have been observed in other DAS datasets, and the scatterers generating these  
 137 chevrons have been inferred to be faults (Lindsey et al., 2019; Spica et al., 2020). More-  
 138 over, these scattered surface waves are also visible in empirical Green’s functions derived  
 139 in DAS datasets that can be migrated to infer scatterer locations (Cheng et al., 2021;  
 140 Y. Yang, Zhan, et al., 2022).

141 Our contributions in this paper are as follows. We suggest a local backprojection  
 142 framework for the systematic location of the sources of these chevron-like features and  
 143 find a strong spatial correlation between these locations and mapped faults. We suggest  
 144 a model of these scatterers as rectangular perturbations in the velocity field, approxi-  
 145 mating a fault zone, and show that this model reproduces first-order features observed  
 146 in the data. We then show that we can constrain key geometric features of the fault zone  
 147 under this backprojection framework.

## 148 2 Data

149 In early July 2019, a large earthquake sequence initiated in the Eastern Califor-  
 150 nia Shear Zone. This sequence, which included a  $M_w$ 6.4 foreshock and a  $M_w$ 7.1 main-  
 151 shock, produced thousands of aftershocks over the course of a few months. Shortly fol-

152 lowering the mainshock, a DAS array was deployed in Ridgecrest, CA using an Optasense  
153 ODH3 interrogator unit in an effort to record this aftershock sequence (Li et al., 2021).  
154 This DAS array began recording on July 10, 2019, and in this study we use recorded af-  
155 tershocks that took place between the initiation of recording and October 4, 2019. The  
156 array is temporally sampled at 250 Hz and is spatially sampled at 8 m intervals over 1250  
157 channels, with a total cable length of 10 km. The deployment of this DAS array ensured  
158 that numerous Ridgecrest sequence aftershocks were recorded nearby at a high spatial  
159 frequency.

160 For this study, we choose a subset of well-recorded, low-noise earthquakes on which  
161 we perform our subsequent analysis. We choose these earthquakes using straightforward  
162 quality control metrics to ensure that scattered surface waves have a high enough signal-  
163 to-noise ratio to be reliably analyzed and that the scattered surface waves are isolated  
164 from any cultural noise that may bias the analysis. As part of this quality control, we  
165 select from only events with  $M_l \geq 2$  or  $M_w \geq 2$  as determined by the Southern Cali-  
166 fornia Seismic Network catalog. We also restricted our selection to only events that oc-  
167 curred between 11 pm and 4 am local time, thus only keeping events with a low prob-  
168 ability of being partially masked by cultural noise. We then manually inspected all of  
169 the remaining events and ensured that we only kept events with negligible cultural noise.  
170 After performing this processing, we are left with 50 events that meet our quality con-  
171 trol criteria. These events are plotted in geographic context in Figure 1. These events  
172 are reasonably well clustered by distance and azimuth, minimizing variability due to the  
173 directional sensitivity of DAS.

### 174 **3 Mapping faults using local backprojection**

175 To quantify the magnitudes and locations of these scatterers, we employ a simple  
176 local backprojection technique to identify the locus points of the scattered waves in the  
177 body wave coda. This backprojection is based on the reasonable assumption that these  
178 chevron-like waves are surface waves generated by earthquake body waves impinging on  
179 a scatterer near the DAS array. We expect this phenomenon to be body-to-surface wave  
180 scattering because the scattered waves are dispersive, which we verify subsequently, and  
181 the onset of these waves occurs early in the body wave coda. We expect these scatter-  
182 ers to be local because the scattered waves attenuate rapidly in space, as exemplified by  
183 the narrow width of these chevrons shown in Figure 1. A schematic example of the gener-  
184 ation of these scattered waves is shown in Figure 2. The driving principle of this method-  
185 ology is the same for standard backprojection techniques used in seismology (Kiser &  
186 Ishii, 2017). In particular, for grid points near or above a scatterer, the backscattered  
187 energy resultant from the scatterer will align and sum coherently, producing a larger am-  
188 plitude than that of a grid point far from any scatterers. In this case, we attempt to back-  
189 project locally scattered surface waves to image the scattering source, illustrated as a  
190 fault zone in Figure 2.

191 To accomplish this backprojection, we first bandpass our data to a narrow frequency  
192 band; this frequency band can vary depending on the desired dimensional sensitivity. We  
193 select frequency bands with 1 Hz widths and center frequencies spanning 2-10 Hz at 0.5  
194 Hz intervals. For each of these frequency bands, we partition the earthquake wavefield  
195 by velocity in the curvelet domain (Atterholt et al., 2021), using a curvelet basis to mute  
196 sections of the frequency-wavenumber domain and thus isolate desired wavefield com-  
197 ponents. This is equivalent to frequency-wavenumber filtering with specialized tapers that  
198 minimized velocity filtering artifacts. We use this wavefield-partitioning technique to se-  
199 parate the scattered wavefield and the direct waves into two separate windows. We clas-  
200 sify velocities below 750 m/s to be the scattered wavefield and velocities above 1000 m/s  
201 to be the direct wavefield. Of the scattered wavefield, we select only the scattered waves  
202 from the early-onset body waves, because these early-onset scattered waves are typically  
203 more pronounced relative to the earthquake wavefield and are not convolved with earthquake-

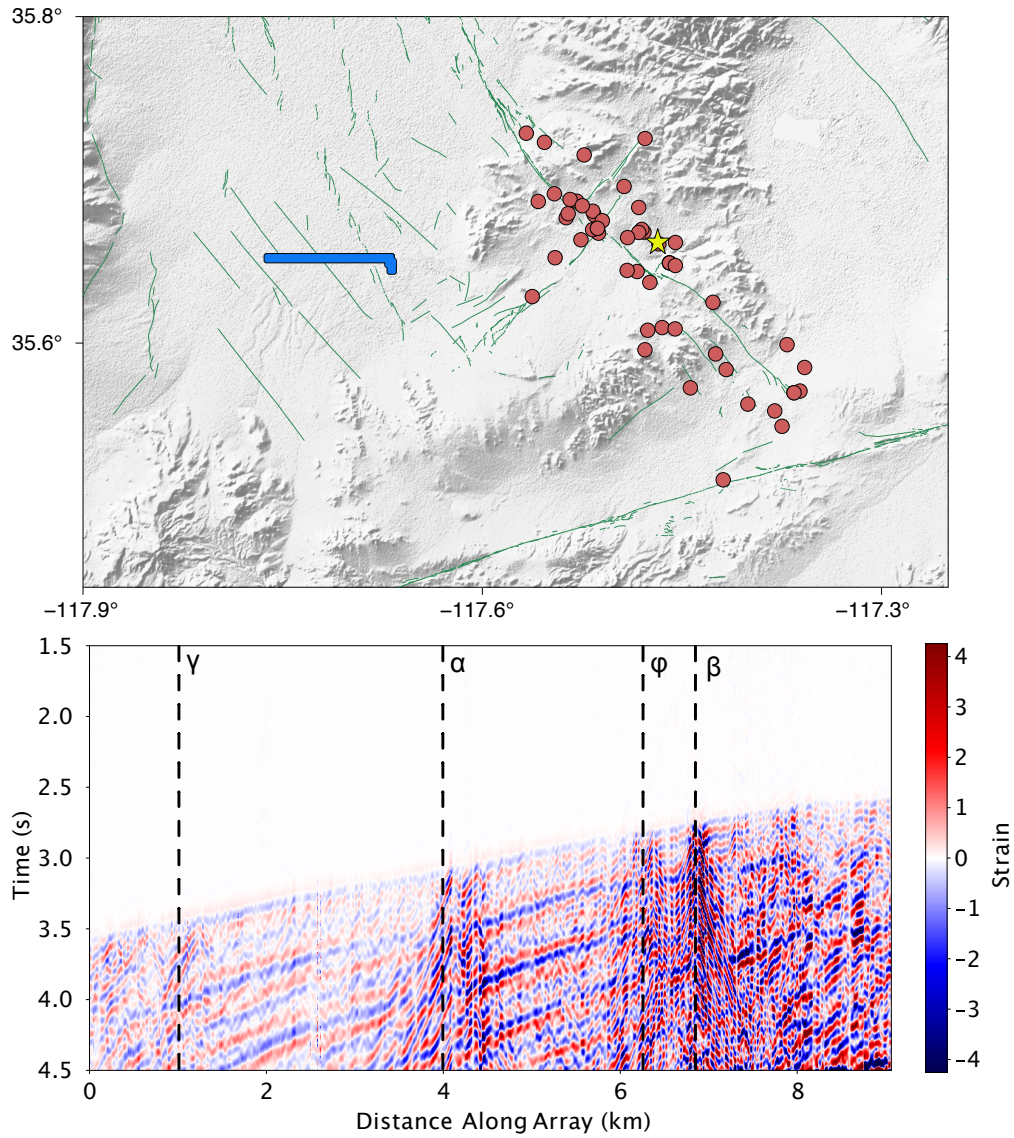


**Figure 1.** Top: The geographic setting of the data used in this study. Blue line corresponds to the DAS array. Red dots correspond to the epicenters of the events used in this study. Yellow star corresponds to the epicenter of the event shown below (depth 5.6 km). Green lines correspond to the USGS-mapped Quaternary faults in the area. Bottom: Example of the DAS-measured wavefield of the onset of an event used in this study. Black dotted lines correspond to the locations of the chevron-like features that are mapped in Figure 3.

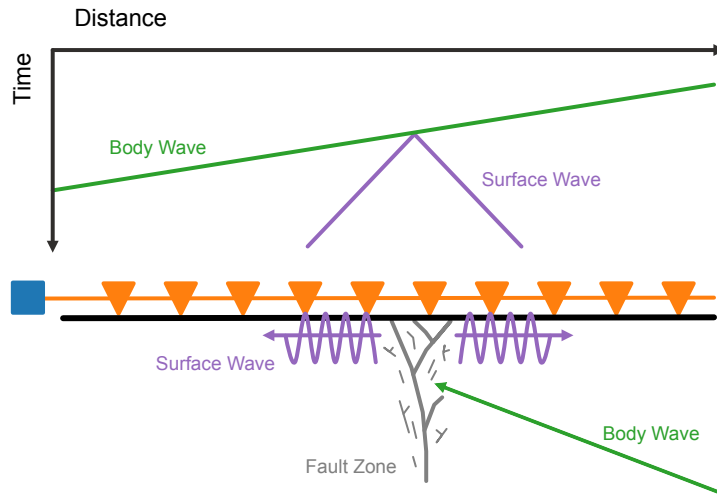


**Figure 2.** Schematic illustration of the phenomena observed in the earthquake wavefields used in this study. Top: Record section corresponding to the processes illustrated below. Bottom: Illustration of the phenomena resulting in the generation of the chevron-like features shown in Figure 1. Colors represent the same phenomena in both top and bottom. Green corresponds to incident body wave. Gray features indicate a fault zone. Purple corresponds to the scattered surface waves resulting from the body waves impinging on the fault zone. Orange line and triangles indicate the fiber optic cable and stations, respectively. Blue box represents the DAS interrogator unit.

204 generated surface waves, which can bias the final result. To isolate the early-onset scattered  
 205 waves, we window the scattered wavefield over the time interval between 2 seconds  
 206 prior to the onset of the P-wave and 5 seconds after the onset of the P-wave. Once we  
 207 have isolated the scattered waves, we perform a local backprojection of surface wave energy  
 208 according to a local velocity model across the array. For the local velocity model,  
 209 we use a 1-dimensional velocity model made by taking averages of each period of the velocity  
 210 model developed by Y. Yang, Atterholt, et al. (2022). We perform this averaging  
 211 to avoid biasing of the result due to lateral slopes in the model. We then define a grid  
 212 of potential scattering sources along the array geometry, and we backproject the surface  
 213 waves recorded by the surrounding channels, up to a fixed distance, according to their  
 214 distance from the potential source. Our grid of potential source locations is spaced at  
 215 8 m along the array, which coincides with the station spacing. In this study, by inspecting  
 216 the data, we fix the maximum distance to be 250 m based on the expected distance  
 217 from the chevron center over which we can expect to get significant constructive interference  
 218 by aligning the waveforms. We then stack the backprojected channels and sum  
 219 the absolute value of the stack, giving us an amplitude for the grid point. We only define  
 220 the grid at the surface along the array, because linear DAS array geometry poorly  
 221 constrains backprojection images along orthogonal axes. But, the rapid attenuation of  
 222 these surface waves suggests that most of the energy in the scattered wavefield is generated  
 223 very close to the array, minimizing the consequence of this poor constraint. Furthermore,  
 224 scattered waves from more distant scatterers will have higher apparent velocities, minimizing  
 225 the impact of these scatterers in a backprojection framework that uses true velocity.  
 226

227 We can verify that these scattered waves are dispersive under this framework. That  
 228 is, we apply this backprojection framework to the earthquake wavefield shown in Fig-

229 ure 1 over a range of velocities for each frequency, rather than using a single velocity model.  
230 We can then sum across each resultant profile to get a single value for each frequency  
231 and velocity pair. From this we can determine which velocities produce the largest sum  
232 at each frequency, which we expect to be correlated with the amount of constructive in-  
233 terference due to waveform alignment. In this way we can construct a dispersion curve  
234 using only the scattered wavefield. This is a similar approach to that taken by Spica et  
235 al. (2022), but because we sum across the entire profile, this produces a velocity spec-  
236 trum that averages the contributions of the scattered waves produced across the array.  
237 A plot of this velocity spectrum is shown in Figure S1. This spectrum shows a clear dis-  
238 persion pattern that is well matched by the dispersive relationship for this setting com-  
239 puted in Y. Yang, Atterholt, et al. (2022).

240 Since DAS measures longitudinal strain, which is distinct from conventional inertial  
241 seismometers, the sensitivity of DAS to these scattered waves is also distinct. For  
242 surface waves generated by scattering from a fault that runs orthogonal to the array, the  
243 recorded surface waves will propagate parallel to the fiber. Consequently, a significant  
244 component of the particle motion will be parallel to the fiber, motion to which DAS is  
245 most sensitive. For a fault that runs oblique to the array, the surface waves will not prop-  
246 agate exactly parallel to the fiber, and the apparent velocity will increase and the sen-  
247 sitivity of the DAS array to the waves will decrease. However, since these waves atten-  
248 uate rapidly in space, the majority of the recorded energy will have been scattered very  
249 close to the array, minimizing variability due to obliquity. Additionally, because DAS  
250 is more sensitive to lower velocities, surface waves are amplified in DAS data relative to  
251 the other components of the earthquake wavefield. This potentially explains why these  
252 surface waves are such a common and well-recorded observation in DAS data (e.g. Lind-  
253 sey et al., 2019; Spica et al., 2020; Ajo-Franklin et al., 2022). These factors suggest that  
254 the variability in scattered waves measured across the DAS array is largely due to vari-  
255 ability in the strength and geometry of the scatterers near the array. Additionally, be-  
256 cause we’re using array seismology, we need to consider apparent velocity when perform-  
257 ing velocity filtering and backprojecting these waves. But, since the recorded surface waves  
258 propagate approximately parallel to the fiber, the apparent velocity of locally scattered  
259 surfaces waves is very close to the true velocity. In particular, the apparent velocity fol-  
260 lows  $v_t/\cos(\theta)$ ; where  $v_t$  is the true velocity and  $\theta$  is the incident angle relative to the  
261 array geometry. In the case of surface waves scattered very close to the array,  $\theta$  is close  
262 to zero.

263 We apply this backprojection technique to the 50 high quality events recorded by  
264 the DAS array in Ridgecrest, CA described in the preceding section. Backprojecting the  
265 scattered wavefields of these earthquakes results in an ensemble of profiles of scattering  
266 across the Ridgecrest DAS array. To ensure that the within-array and between-event am-  
267 plitudes are comparable, we normalize the profile amplitudes by the sum of the abso-  
268 lute value of the body waves that occupy the same window used for each grid point in  
269 each profile. For this normalization, we account for the variability in azimuth and in-  
270 cident angle according to the directional sensitivity of strainmeters (Benioff, 1935). In  
271 particular, noting that the dominant body wave signal we use for this normalization is  
272 the P-wave, we divide the direct wavefield by  $\cos^2(\theta)$ . We smooth these profiles with a  
273 Gaussian kernel with a standard deviation of 5 channels to minimize any high-frequency,  
274 stochastic variability in these profiles. We show these ensembles of backprojection pro-  
275 files computed at 4 and 7 Hz center frequencies in Figure 3. These profiles are generally  
276 ”bumpy,” and it can be difficult to determine to which of these peaks to assign signifi-  
277 cance. Additionally, some peaks are of low amplitude, but are noteworthy because they  
278 are positioned in areas with low noise floors. To help us determine which peaks are most  
279 likely associated with scatterers, we use the metric from mountaineering of topographic  
280 prominence, which is a measure of the height of a peak relative to its surroundings. We  
281 plot the prominence profiles alongside the backprojection amplitude profiles in Figure  
282 3. Additionally, we superimpose these prominence profiles on the DAS array geometry

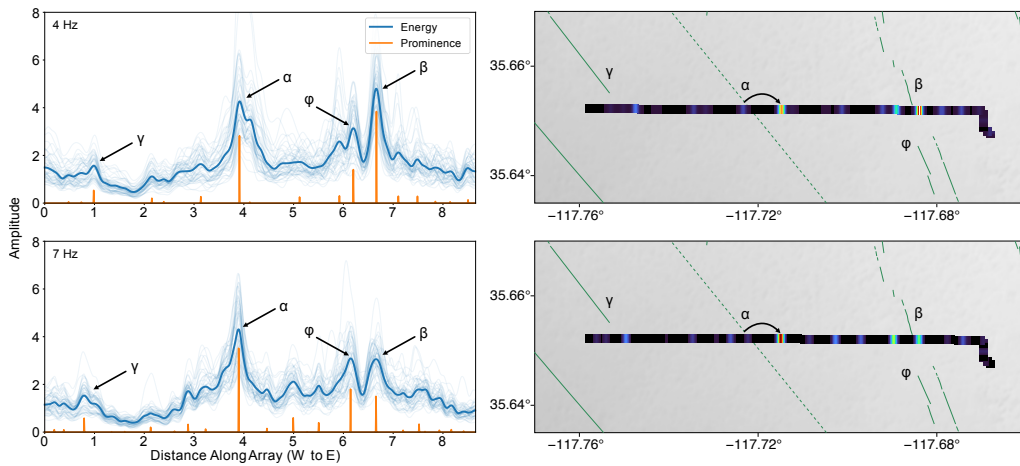


**Figure 3.** Left: Backprojection profiles made using 50 events recorded by the DAS array in Ridgecrest, CA. Light blue lines correspond to profiles made using a single event. Dark blue lines correspond to the mean profile. Orange lines correspond to the topographic prominence of the mean energy profile. Top and bottom plots correspond to profiles generated with 4 and 7 Hz center frequencies, respectively. Black arrows point to referenced peaks  $\alpha$ ,  $\beta$ ,  $\gamma$ , and  $\phi$ . Right: Prominence profiles to the left, convolved with Gaussian kernel to widen peaks for representation, plotted on the DAS array geometry shown in Figure 1. Color corresponds to prominence amplitude. Green lines correspond to fault locations. Solid lines are moderately or well constrained fault locations, and dotted lines are inferred fault locations. Faults are labeled according to associated peaks indicated in the profiles to the left. Curved black arrows indicate the proposed relocation of the fault associated with peak  $\alpha$ .

283 in Figure 3. Indeed, there is a spatial correlation between peaks in the prominence pro-  
 284 file and the locations of USGS-mapped Quaternary faults near the array. This spatial  
 285 correlation partially evidences the argument that the nearly ubiquitous chevron-like fea-  
 286 tures in the DAS measured wavefield are fault-zone scattered waves. In Figure 3, we make  
 287 note of four peaks, which we term peaks  $\alpha$ ,  $\beta$ ,  $\gamma$ , and  $\phi$ . These are the most prominent  
 288 peaks in both frequency bands, and by visual inspection we can associate these peaks  
 289 with mapped faults nearby. In particular, peaks  $\alpha$  and  $\beta$  are noteworthy in that they  
 290 are prominent enough that we can analyze their behavior with space and frequency. We  
 291 use peaks  $\alpha$  and  $\beta$  to infer properties of the associated fault zones subsequently.

#### 292 4 Modeling scatterers as fault zones

293 To further investigate the nature of the sources of scattering evident in DAS data,  
 294 we present a model for these scatterers as rectangular perturbations in the 2D velocity  
 295 structure. Although natural faults are neither perfect rectangles nor uniform velocity per-  
 296 turbations, this simple parameterization allows us to capture first order structural prop-  
 297 erties of fault zones without including more complexity than we can feasibly resolve given  
 298 our data. The few free parameters of this fault model are burial depth, maximum depth,  
 299 width, and percent change in velocity. For a background velocity model, we use a com-  
 300 bination of the aforementioned shear wave velocity model from Y. Yang, Atterholt, et  
 301 al. (2022) for the shallowest 150 m and a local 1D velocity profile taken from the SCEC  
 302 Unified Community Velocity Model (Small et al., 2017) for depths deeper than 150 m;  
 303 we combine these two models using a linear interpolation. We then create a model fault

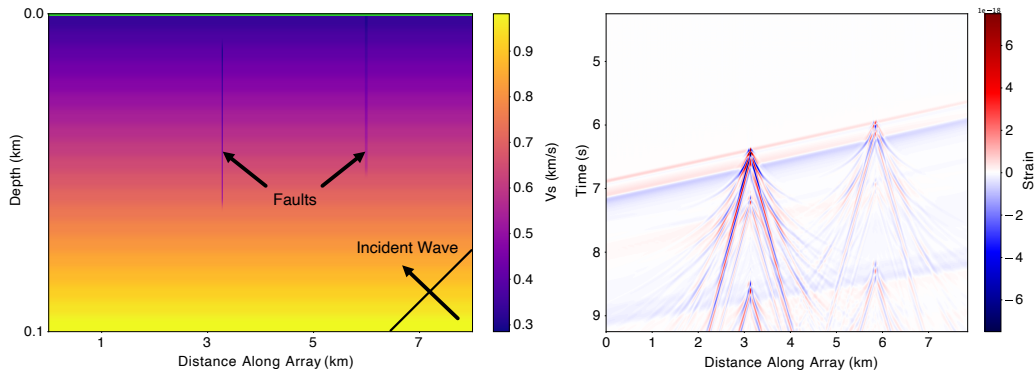


**Figure 4.** Left: Example of velocity model modified from (Y. Yang, Atterholt, et al., 2022) and (Small et al., 2017) with two fault zone-approximating velocity perturbations emplaced in the model. Green line corresponds to array of strainmeters. Black arrows point to incident wave direction and fault locations. Note the large vertical exaggeration. Right: Record section generated from scenario illustrated to the left.

304 zone by multiplying a section of the background model with an assigned rectangular ge-  
 305 ometry by a constant of proportionality.

306 We then use this model to perform synthetic tests that we can compare to our ob-  
 307 servations to assess the feasibility of this scatterer model. We generate these synthe-  
 308 tics using Salvus (Afanasiev et al., 2019), a full waveform modeling software that simu-  
 309 lates wave propagation using the spectral element method. We approximate the DAS  
 310 array at Ridgecrest as a linear, 8 km array of strainmeters at the surface of our Earth  
 311 model. We emplace a 2D double couple source with a 0.1 s half-duration Gaussian rate  
 312 source time function 30 km east of the array at 10 km depth, a representative distance  
 313 and depth for the earthquakes used in this study. We generate an adaptive mesh with  
 314 which we can compute these synthetics up to 10.5 Hz with at least one element per wave-  
 315 length. We use the same setup to perform tests of the fault geometry that we describe  
 316 subsequently. We show an example of a simulation for a model with two faults with dif-  
 317 ferent geometries and velocity reductions in Figure 4. The faults in Figure 4 were pa-  
 318 rameterized using models for the faults associated with scatterers  $\alpha$  and  $\beta$  that are pro-  
 319 posed in the subsequent section. In particular, the fault on the left is parameterized as  
 320 a 30% velocity reduction with a width of 20 m and a depth extent of 10 to 60 m. The  
 321 fault on the right is parameterized as a 10% velocity reduction with a width of 50 m and  
 322 a depth extent of 0 to 50 m. Both fault parameterizations are vertical. The resultant scat-  
 323 tered waves in the synthetic wavefield match many of the first-order characteristics of  
 324 the scattered waves in the observations of Figure 1. In particular, we have reproduced  
 325 the observation of low-velocity scattered surface waves emanating from a narrow source.  
 326 We can evaluate the similarities in the velocity content of the synthetic data and the ob-  
 327 served data by computing the velocity spectrum of the scatterer component of the syn-  
 328 thetic wavefield, as outlined in the preceding section. We show the velocity spectrum in  
 329 Figure S2. The dispersion of the scattered wavefield in the synthetic test is a close match  
 330 to the dispersion for the real data in Figure S1. These simulations thus further confirm  
 331 that these scatterers may be related to faults. As is clear in Figure 4, variations in the  
 332 properties of the model fault zones create visually apparent differences in the strength  
 333 of the scattered wavefield.

## 5 Constraining fault geometry

Now that we have a method of quantifying the degree of scattering in data and a means of simulating our observations using a reasonable model, we can constrain the properties of the sources of scattered waves by comparing features between the data and synthetics under this backprojection framework. As is evident in Figure 3, the peaks in these backprojection profiles have variant properties in space and frequency, and this variability may inform a better understanding of the faults that generate these peaks. Moreover, since we performed this backprojection for many events, we have an ensemble of profiles with which we can evaluate how well constrained the fault-zone properties that control these peak shapes are.

To generate our synthetics, we use the velocity model and source described in the preceding section. We also incorporate attenuation into our model. Since we do not have a priori estimates of the attenuation at this site, we parameterize the attenuation using the functional decay of the peaks from our backprojection profiles to obtain a rough estimate of the local attenuation structure. We assume an empirical relationship between shear wave velocity and attenuation structure, a common assumption when building an Earth model with heterogeneous attenuation structure (Graves & Pitarka, 2010), and may be denoted as  $Q_\mu = cV_s$ . To test the attenuation of surface waves away from a local scatterer, we define a fault zone according to the aforementioned simplified fault model with a width of 20 m, a depth extent of 0-100 m, and a 30% velocity reduction. We test several values for  $c$  and compare the spatial decay of the resultant synthetic peaks to those of peaks  $\alpha$  and  $\beta$  at 4 Hz. We find that the data are best fit by a value of  $c = 50$ , a reasonable value for this relationship (Lin & Jordan, 2018; Lai et al., 2020). These peak comparisons are shown in Figure S3. This empirical relationship between attenuation and velocity is imperfect, as other parameters such as temperature and fluid content also control attenuation (Brocher, 2008; Eberhart-Phillips et al., 2014), and other factors such as structural heterogeneity can control surface wave amplitude (Bowden & Tsai, 2017). But, since we are only trying to obtain a reasonable attenuation parameterization for our forward model, this approximation is sufficient for our purposes.

To constrain the local fault zone properties, we note that the backprojection profiles shown in Figure 3 are functions of the frequency band in which we filter the data, and that each peak behaves differently with frequency. We investigate this property by evaluating the backprojection profiles for all narrow frequency bands for which we computed profiles in this study, with center frequencies ranging from 2 to 10 Hz. By plotting the mean profiles at each center frequency together, we can better inform our understanding of the behavior of the frequency dependence of individual scattering features along the array. We plot these mean profiles against center frequency and distance as a pseudocolor plot in Figure 5. As is evident in Figure 5, there are peaks that are traceable across a range of center frequencies, and there is a high degree of variability in the behavior of these peaks with frequency.

We then focus on the two most prominent peaks in this image, peak  $\alpha$  and peak  $\beta$ , both of which are spatially correlated with USGS-mapped faults (USGS & CGS, 2022). By taking cross sections of the center frequency versus distance along array plot, we can determine the frequency dependence of these specific scatterers along this profile. Clearly, these peaks have different frequency dependences, which likely reflects a variability in the depth and geometry of the scattering fault zone. To discern the properties of these faults, we test different fault zone geometries to match these frequency dependent trends. Because the amplitudes of DAS data are not well understood, we only attempt to match the shape of the synthetic profile with the shapes of the peak profiles, and we thus normalize the synthetic profile amplitude by the ratio of the integrated amplitude of the mean peak profile to the integrated amplitude of the synthetic peak profile. We attempted to reproduce these frequency-amplitude trends by performing synthetic simulations that included fault zones with varying free parameters. These simulations were too expen-

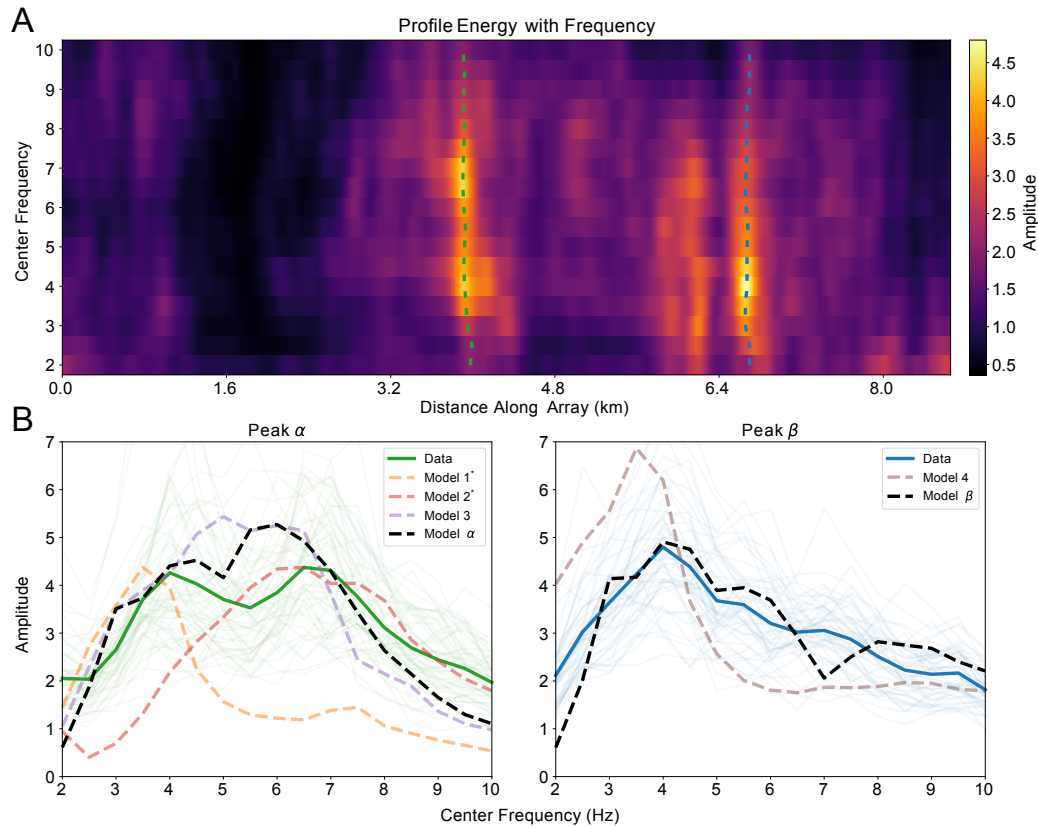


**Figure 5.** A. Pseudocolor plot of mean backprojection amplitude plotted against center frequency and distance along array. Dotted green and dotted blue lines correspond to cross sections of this plot, associated with peaks  $\alpha$  and  $\beta$ , respectively. B. Plots of backprojection amplitude versus center frequency for the cross-sections shown in A. Light green and light blue lines are the frequency-amplitude curves determined for a single event for peaks  $\alpha$  and  $\beta$ , respectively. Dark green and dark blue lines are the mean frequency amplitude curves for peaks  $\alpha$  and  $\beta$ , respectively. Dotted black lines correspond to the frequency-amplitude curves for our preferred fault zone model for each peak. Dotted colored lines are frequency amplitude curves for fault zone models with variant parameters to illustrate the constraints of this methodology. The parameters used for each model are given in Table S1. The asterisk in the legend indicates that, for visualization purposes, the corresponding model is normalized by the maximum height of the data curve rather than the integrated sum.

387 sive to perform a full grid search over all the fault model parameters, but by identify-  
388 ing patterns between fault zone parameterizations and subsequent simulated frequency-  
389 amplitude profiles, we were able to find fault zone models that produced good fits to the  
390 profile ensembles for both faults, as shown in Figure 5B. Indeed, reproducing the frequency-  
391 amplitude curves for the different peaks requires the use of variant fault zone parame-  
392 terizations. Peak  $\alpha$  is best fit by a 30% velocity reduction that is 20 m wide and spans  
393 10 to 60 m depths. Peak  $\beta$  is best fit by a 10% velocity reduction that is 50 m wide and  
394 spans 0 to 50 m depths. The results for peak  $\alpha$  suggest that we may be able to detect  
395 and constrain properties of small-scale buried faults.

## 396 6 Discussion

397 The spatial correlation between the locations of sources of scattering and the mapped  
398 faults near the Ridgecrest DAS array shown in Figure 3 suggests that the source of at  
399 least some of these scatterers are faults, and thus DAS arrays can detect measurable sig-  
400 natures of fault zones. An example of the potential utility of this technique is readily avail-  
401 able in this dataset. In particular, peak  $\alpha$  is located near, but is offset from, a mapped  
402 fault extending across the array. The Quaternary Fault Catalog (USGS & CGS, 2022)  
403 records this fault's location as inferred rather than directly observed; thus, we can use  
404 our backprojection profile to refine the location of this fault, treating peak  $\alpha$  as a po-  
405 tential node of the fault trace. This node provides a stronger constraint on this fault's  
406 location near the town of Ridgecrest, CA, which has important implications for the lo-  
407 cation of possible static strain in the event of the activation of the Little Lake Fault Zone.  
408 This technique is generalizable to all DAS arrays that record seismicity, and may then  
409 be used elsewhere to systematically refine inferred fault locations and suggest the pres-  
410 ence and locations of previously unmapped faults.

411 The profiles in Figure 3 bear a resemblance to results from distinct fault zone char-  
412 acterization methodologies, namely S-wave amplification analysis (e.g. Qiu et al., 2021).  
413 Both techniques can be used to locate faults at small spatial scales using the peak lo-  
414 cations, but these techniques otherwise provide complimentary information. For exam-  
415 ple, the shape of the peaks in S-wave amplification profiles can be interpreted as an es-  
416 timate of the lateral characteristics of the fault damage zone, while the shape of the peaks  
417 in this study are largely reflective of the processing workflow and amplitude attenuation.  
418 But, the methodology presented in this study is more sensitive to small variations in the  
419 frequency of scattered waves that are reflective of characteristic dimensions of the fault  
420 zone, which includes constraints on the depth-dependence of the fault zone. Addition-  
421 ally, the methodology presented in this study is more readily applicable to DAS, both  
422 because DAS amplitudes are not well understood due to variability in coupling of the  
423 fiber and because DAS is particularly sensitive to low velocity surface waves.

424 The synthetic simulations in this study provide additional evidence that these chevron-  
425 like observations in DAS data are well-explained by fault zones. In particular, as shown  
426 in Figure 4, an approximation of a fault zone as a rectangular perturbation in velocity  
427 reproduces the first order features of these chevron-like observations. Additionally, the  
428 complexity in the frequency-amplitude curves shown in Figure 5 evidences a necessary  
429 variability in the finite properties of the scattering fault zones (Almuhaidib & Toksöz,  
430 2014). But, importantly, this representation is non-unique, and the diversity of geologic  
431 heterogeneity in the upper crust suggests that features other than fault zones are likely  
432 responsible for at least some of the chevron-like observations we see in DAS data.

433 The geometric constraints we place on the faults in this study illustrate that, us-  
434 ing DAS recorded earthquakes, we can constrain some aspects of the subsurface geom-  
435 etry of fault zones on the scale of tens of meters, potentially even for buried faults as is  
436 the case for peak  $\alpha$ . Although these solutions are non-unique, they provide robust con-  
437 straints on the approximate scaling of these subsurface structures. As stated prior, we

438 were able to approach fault models that fit these data by identifying patterns in the re-  
439 lationship between fault zone geometry and the resultant synthetics. One interesting re-  
440 lationship, made clear in Figure 5, is related to the observation that peak  $\beta$  has a uni-  
441 modal frequency-amplitude curve while peak  $\alpha$  has a bimodal frequency-amplitude curve.  
442 The simulations suggest that two characteristic lengths produce distinct modes in these  
443 frequency-amplitude curves: the fault zone width and the fault zone depth extent. In  
444 particular, we obtain a unimodal frequency-amplitude curve when these lengths are the  
445 same (as with peak  $\beta$ ) and a bimodal frequency-amplitude curve when these lengths are  
446 distinct (as with peak  $\alpha$ ), with the smaller characteristic dimension responsible for the  
447 highest frequency mode and vice versa. We demonstrate that variant characteristic di-  
448 mensions can account for each frequency mode of peak  $\alpha$  by running separate simula-  
449 tions for square-shaped buried faults, with velocity perturbations equivalent to the best  
450 fitting model for peak  $\alpha$ , that extend up to 10 m depth with side lengths of 50 m and  
451 20 m, lengths which match the depth extent and width, respectively of the best fitting  
452 model for peak  $\alpha$ . The amplitude-frequency curves of these simulations are plotted as  
453 Models 1 and 2 in Figure 5, respectively. Both of these models well approximate one of  
454 the individual modes of the bimodal data curve for peak  $\alpha$ . Finally, although we nor-  
455 malize by amplitude, the magnitude of the velocity perturbation subtly changes the shape  
456 of the synthetic curves in our simulations in Figure 5; however, this is a weakly constrained  
457 parameter in this methodology.

458 Although this is not the first study to attempt to map fault zones using scattered  
459 waves in DAS data, a key contribution of this study is that it provides a framework to  
460 systematically locate the origins and discern the dimensions of these scatterers using the  
461 earthquake wavefield. Importantly, when using the earthquake wavefield, we are mostly  
462 looking at body-to-surface scattered waves, which have a different depth sensitivity than  
463 surface-to-surface scattered waves. In particular, body-to-surface wave scattering has a  
464 deeper depth sensitivity than surface-to-surface wave scattering because body waves can  
465 propagate at depth while surface waves have a frequency-limited depth extent (Barajas  
466 et al., 2022). But, body-to-surface wave scattering at a given frequency is still only sen-  
467 sitive to depths at which a scattering source can excite surface waves. Differences in sen-  
468 sitivity are important to consider when comparing this methodology to other scatterer  
469 characterization methods that use surface-to-surface wave scattering. Since we can only  
470 feasibly apply this technique between 2-10 Hz, this depth sensitivity constraint suggests  
471 that this methodology is only sensitive to the top few hundred meters. But, we suggest  
472 that the depth extents determined in this study are well-constrained by the data. To il-  
473 lustrate this, we perform a simulation for a fault with the same parameters as the best  
474 fitting model for peak  $\beta$ , but change the depth extent from 0-50 m to 0-100 m. The frequency-  
475 amplitude curve for this simulation is plotted as Model 4 in Figure 5. This curve shows  
476 that for a deeper fault, we would expect to observe a frequency-amplitude curve more  
477 depleted in higher frequencies and enriched in lower frequencies.

478 In Y. Yang, Zhan, et al. (2022), the authors discern properties of the fault zone as-  
479 sociated with peak  $\alpha$  in this study as a 30% velocity reduction that is 35 m wide and  
480 spans 0 to 90 m depths. While this geometry is very close to our result and provides a  
481 useful verification of our technique, the differences that arise are likely due to the dif-  
482 ferent sensitivities of the measurements and the different frequencies used to fit the fault  
483 model. Namely, the geometry of the faults discerned in this study were partially con-  
484 strained by measurements over 6 Hz, which were not used to constrain the geometry in  
485 Y. Yang, Zhan, et al. (2022). The higher frequency content used in this study likely ex-  
486 plains why the characteristic dimensions discerned in this study are both smaller than  
487 those found in Y. Yang, Zhan, et al. (2022). The higher frequency content may account  
488 for our ability to resolve a shallow burial depth. This fault burial depth is largely con-  
489 strained by subtle variations in the peak shape. To illustrate this, we generate synthet-  
490 ics for a fault model with the same parameters as the best fitting model for peak  $\alpha$ , but  
491 use a depth extent of 0-50 m instead of 10-60 m. The frequency-amplitude curve for this

492 synthetic test is plotted as Model 3 in Figure 5. This result shows, that for an unburied  
493 fault, we achieve a slightly different shape that does not capture any separation of the  
494 high and low frequency modes of the data curve for peak  $\alpha$ .

495 Finally we note that, although this study focused on relatively minor faults, this  
496 methodology can be readily extended to major fault zones, and requires only an across-  
497 fault DAS array and earthquake observations. Indeed, since the interrogation length for  
498 DAS units is increasing, and since many in situ fibers cross major faults, we can expect  
499 the number of DAS arrays sensing structure over major fault zones to increase rapidly  
500 over time. The technique presented in this paper presents an opportunity to leverage these  
501 DAS arrays to measure the fracture density and characteristics within major fault zones.  
502 Moreover, this study only covers one method with which DAS can be used to charac-  
503 terize major fault zones. Many of the aforementioned techniques which have previously  
504 used densely deployed conventional seismometers can be performed with DAS. The key  
505 challenges in applying these techniques, however, are that DAS provides a different ob-  
506 servation than traditional seismometers, single component strain, and that DAS ampli-  
507 tudes are not well understood due to variability in coupling. These differences make some  
508 traditional fault characterization techniques, such as detecting fault zone head waves us-  
509 ing particle motion analysis or measuring S-wave amplification, more difficult to apply  
510 using only DAS data. But, including some conventional inertial seismometers along a  
511 DAS array has the potential to diminish some of the challenges of DAS data (e.g. H. F. Wang  
512 et al., 2018; Lindsey et al., 2020; Muir & Zhan, 2021; Y. Yang, Atterholt, et al., 2022).  
513 For the fault zone characterization case, including collocated 3-component seismic sen-  
514 sors allows for amplitude calibration of DAS data and provides local particle motion ob-  
515 servations. In this way, we can leverage the high station density and extensive deploy-  
516 ments of DAS data while minimizing its limitations.

## 517 **7 Conclusions**

518 In this study we present a framework for the systematic location and character-  
519 ization of fault zones using the DAS measured earthquake wavefield. This framework,  
520 which relies on the simple backprojection of the scattered wavefield following an earth-  
521 quake, yields profiles of the scattered wave energy across the array. We apply this frame-  
522 work to 50 earthquake record sections recorded by a DAS array in Ridgecrest, CA, yield-  
523 ing an ensemble of profiles of scattered wave energy across the array. With these pro-  
524 files, we identify numerous scattering peaks that are spatially well-correlated with mapped  
525 faults in the area, suggesting that these observed scattered waves are faults. Using these  
526 backprojection profiles, we suggest a correction to the location of one of the mapped faults  
527 in the area. Moreover, we present a model for these scattering sources as rectangular per-  
528 turbations in the velocity structure, which is a simple approximation of a fault zone, and  
529 through simulations we show that this model reproduces first order observations of the  
530 observed scattered waves. Using this backprojection technique and these simulations,  
531 we establish a framework for using the locally scattered wavefield to evaluate shallow at-  
532 tenuation structure and infer characteristic dimensions of fault zones. We then apply this  
533 framework to the profiles computed for the Ridgecrest DAS array and consequently make  
534 claims about the fault zone structure near the array. We use the frequency decay of the  
535 profile peaks and synthetic simulations to image local faults at the scale of tens of me-  
536 ters, and with these images we distinguish between a fault that is surface-breaching and  
537 a fault that is buried.

## 538 **Open Research**

539 The data used in this study are available online (<https://doi.org/10.22002/D1.20038>) as  
540 30-second record sections that include the initial onset of the earthquake wavefield for  
541 the 50 high signal-to-noise ratio aftershocks recorded by the distributed acoustic sens-

542 ing (DAS) array in Ridgecrest, CA referenced in this study. The simulations performed  
 543 for this study were done using the software Salvus, (Afanasiev et al., 2019), available at  
 544 <https://mondaic.com/>. Figure 1 was made using The Generic Mapping Tools (GMT),  
 545 version 6 (Wessel et al., 2019), available at <https://www.generic-mapping-tools.org/>.

## 546 Acknowledgements

547 This study was made possible by the funding provided by the National Science Founda-  
 548 tion (NSF) through the Faculty Early Career Development (CAREER) award num-  
 549 ber 1848106 and Graduate Research Fellowships Program (GRFP) number DGE-1745301.  
 550 Additional funding was provided by the Braun Trust and the United States Geological  
 551 Survey (USGS) Earthquake Hazards Program (EHP) award number G22AP00067. We  
 552 would also like to thank the California Broadband Cooperative for fiber access for the  
 553 Distributed Acoustic Sensing array used in this experiment.

## 554 References

- 555 Afanasiev, M., Boehm, C., van Driel, M., Krischer, L., Rietmann, M., May, D. A.,  
 556 ... Fichtner, A. (2019). Modular and flexible spectral-element waveform model-  
 557 ling in two and three dimensions. *Geophysical Journal International*, 216(3),  
 558 1675–1692. doi: 10.1093/gji/ggy469
- 559 Ajo-Franklin, J., Tribaldos, V. R., Nayak, A., Cheng, F., Mellors, R., Chi, B., ...  
 560 Dobson, P. (2022). The Imperial Valley Dark Fiber Project: Toward Seismic  
 561 Studies Using DAS and Telecom Infrastructure for Geothermal Applications. ,  
 562 14.
- 563 Allam, A. A., Ben-Zion, Y., & Peng, Z. (2014, November). Seismic Imaging of a  
 564 Bimaterial Interface Along the Hayward Fault, CA, with Fault Zone Head  
 565 Waves and Direct P Arrivals. *Pure and Applied Geophysics*, 171(11), 2993–  
 566 3011. Retrieved 2022-01-13, from [http://link.springer.com/10.1007/  
 567 s00024-014-0784-0](http://link.springer.com/10.1007/s00024-014-0784-0) doi: 10.1007/s00024-014-0784-0
- 568 Almuheidib, A. M., & Toksöz, M. N. (2014, July). Numerical modeling of elastic-  
 569 wave scattering by near-surface heterogeneities. *GEOPHYSICS*, 79(4), T199–  
 570 T217. Retrieved 2022-06-17, from [https://library.seg.org/doi/10.1190/  
 571 geo2013-0208.1](https://library.seg.org/doi/10.1190/geo2013-0208.1) doi: 10.1190/geo2013-0208.1
- 572 Amos, C. B., Brownlee, S. J., Rood, D. H., Fisher, G. B., Burgmann, R., Renne,  
 573 P. R., & Jayko, A. S. (2013, July). Chronology of tectonic, geomorphic, and  
 574 volcanic interactions and the tempo of fault slip near Little Lake, California.  
 575 *Geological Society of America Bulletin*, 125(7-8), 1187–1202. Retrieved 2022-  
 576 06-01, from [https://pubs.geoscienceworld.org/gsabulletin/article/  
 577 125/7-8/1187-1202/125934](https://pubs.geoscienceworld.org/gsabulletin/article/125/7-8/1187-1202/125934) doi: 10.1130/B30803.1
- 578 Ampuero, J., Vilotte, J., & Sánchez-Sesma, F. J. (2002, December). Nucleation of  
 579 rupture under slip dependent friction law: Simple models of fault zone. *Jour-  
 580 nal of Geophysical Research: Solid Earth*, 107(B12), ESE 2–1–ESE 2–19. Re-  
 581 trieved 2022-01-11, from <http://doi.wiley.com/10.1029/2001JB000452> doi:  
 582 10.1029/2001JB000452
- 583 Atterholt, J., Zhan, Z., Shen, Z., & Li, Z. (2021, November). A unified wavefield-  
 584 partitioning approach for distributed acoustic sensing. *Geophysical Journal In-  
 585 ternational*, 228(2), 1410–1418. Retrieved 2021-12-09, from [https://academic  
 586 .oup.com/gji/article/228/2/1410/6382997](https://academic.oup.com/gji/article/228/2/1410/6382997) doi: 10.1093/gji/ggab407
- 587 Barajas, A., Margerin, L., & Campillo, M. (2022, April). Coupled body and surface  
 588 wave sensitivity kernels for coda-wave interferometry in a three-dimensional  
 589 scalar scattering medium. *Geophysical Journal International*, 230(2), 1013–  
 590 1029. Retrieved 2022-06-17, from [https://academic.oup.com/gji/article/  
 591 230/2/1013/6545800](https://academic.oup.com/gji/article/230/2/1013/6545800) doi: 10.1093/gji/ggac091
- 592 Benioff, H. (1935, October). A linear strain seismograph. *Bulletin of the Seis-*

- 593 *mological Society of America*, 25(4), 283–309. Retrieved 2022-01-06, from  
 594 [https://pubs.geoscienceworld.org/ssa/bssa/article/25/4/283/115110/](https://pubs.geoscienceworld.org/ssa/bssa/article/25/4/283/115110/A-linear-strain-seismograph)  
 595 [A-linear-strain-seismograph](https://pubs.geoscienceworld.org/ssa/bssa/article/25/4/283/115110/A-linear-strain-seismograph) doi: 10.1785/BSSA0250040283
- 596 Bense, V., Gleeson, T., Loveless, S., Bour, O., & Scibek, J. (2013, December).  
 597 Fault zone hydrogeology. *Earth-Science Reviews*, 127, 171–192. Retrieved  
 598 2022-06-20, from [https://linkinghub.elsevier.com/retrieve/pii/](https://linkinghub.elsevier.com/retrieve/pii/S0012825213001657)  
 599 [S0012825213001657](https://linkinghub.elsevier.com/retrieve/pii/S0012825213001657) doi: 10.1016/j.earscirev.2013.09.008
- 600 Ben-Zion, Y., Peng, Z., Okaya, D., Seeber, L., Armbruster, J. G., Ozer, N., ... Ak-  
 601 tar, M. (2003, March). A shallow fault-zone structure illuminated by trapped  
 602 waves in the Karadere-Duzce branch of the North Anatolian Fault, western  
 603 Turkey. *Geophysical Journal International*, 152(3), 699–717. Retrieved 2022-  
 604 02-17, from [https://academic.oup.com/gji/article-lookup/doi/10.1046/](https://academic.oup.com/gji/article-lookup/doi/10.1046/j.1365-246X.2003.01870.x)  
 605 [j.1365-246X.2003.01870.x](https://academic.oup.com/gji/article-lookup/doi/10.1046/j.1365-246X.2003.01870.x) doi: 10.1046/j.1365-246X.2003.01870.x
- 606 Bowden, D. C., & Tsai, V. C. (2017, January). Earthquake ground motion ampli-  
 607 fication for surface waves: Ground Motions for Surface Waves. *Geophysical Re-*  
 608 *search Letters*, 44(1), 121–127. Retrieved 2022-06-13, from [http://doi.wiley](http://doi.wiley.com/10.1002/2016GL071885)  
 609 [.com/10.1002/2016GL071885](http://doi.wiley.com/10.1002/2016GL071885) doi: 10.1002/2016GL071885
- 610 Brocher, T. M. (2008, April). Key elements of regional seismic velocity models  
 611 for long period ground motion simulations. *Journal of Seismology*, 12(2), 217–  
 612 221. Retrieved 2022-06-20, from [http://link.springer.com/10.1007/s10950-](http://link.springer.com/10.1007/s10950-007-9061-3)  
 613 [-007-9061-3](http://link.springer.com/10.1007/s10950-007-9061-3) doi: 10.1007/s10950-007-9061-3
- 614 Catchings, R. D., Goldman, M. R., Li, Y., & Chan, J. H. (2016, December). Con-  
 615 tinuity of the West Napa–Franklin Fault Zone Inferred from Guided Waves  
 616 Generated by Earthquakes Following the 24 August 2014  $M_w$  6.0 South Napa  
 617 Earthquake. *Bulletin of the Seismological Society of America*, 106(6), 2721–  
 618 2746. Retrieved 2022-02-17, from [https://pubs.geoscienceworld.org/bssa/](https://pubs.geoscienceworld.org/bssa/article/106/6/2721-2746/324905)  
 619 [article/106/6/2721-2746/324905](https://pubs.geoscienceworld.org/bssa/article/106/6/2721-2746/324905) doi: 10.1785/0120160154
- 620 Cheng, F., Chi, B., Lindsey, N. J., Dawe, T. C., & Ajo-Franklin, J. B. (2021, De-  
 621 cember). Utilizing distributed acoustic sensing and ocean bottom fiber  
 622 optic cables for submarine structural characterization. *Scientific Reports*,  
 623 11(1), 5613. Retrieved 2022-01-11, from [http://www.nature.com/articles/](http://www.nature.com/articles/s41598-021-84845-y)  
 624 [s41598-021-84845-y](http://www.nature.com/articles/s41598-021-84845-y) doi: 10.1038/s41598-021-84845-y
- 625 Cochran, E. S., Li, Y.-G., Shearer, P. M., Barbot, S., Fialko, Y., & Vidale, J. E.  
 626 (2009, April). Seismic and geodetic evidence for extensive, long-lived fault  
 627 damage zones. *Geology*, 37(4), 315–318. Retrieved 2022-06-01, from  
 628 [http://pubs.geoscienceworld.org/geology/article/37/4/315/29883/](http://pubs.geoscienceworld.org/geology/article/37/4/315/29883/Seismic-and-geodetic-evidence-for-extensive)  
 629 [Seismic-and-geodetic-evidence-for-extensive](http://pubs.geoscienceworld.org/geology/article/37/4/315/29883/Seismic-and-geodetic-evidence-for-extensive) doi: 10.1130/G25306A.1
- 630 Eberhart-Phillips, D., Thurber, C., & Fletcher, J. B. (2014, October). Imaging P  
 631 and S Attenuation in the Sacramento-San Joaquin Delta Region, Northern  
 632 California. *Bulletin of the Seismological Society of America*, 104(5), 2322–  
 633 2336. Retrieved 2022-06-20, from [https://pubs.geoscienceworld.org/bssa/](https://pubs.geoscienceworld.org/bssa/article/104/5/2322-2336/351484)  
 634 [article/104/5/2322-2336/351484](https://pubs.geoscienceworld.org/bssa/article/104/5/2322-2336/351484) doi: 10.1785/0120130336
- 635 Ellsworth, W. L. (2013, July). Injection-Induced Earthquakes. *Science*, 341(6142),  
 636 1225942. Retrieved 2022-06-01, from [https://www.science.org/doi/](https://www.science.org/doi/10.1126/science.1225942)  
 637 [10.1126/science.1225942](https://www.science.org/doi/10.1126/science.1225942) doi: 10.1126/science.1225942
- 638 Faulkner, D., Jackson, C., Lunn, R., Schlische, R., Shipton, Z., Wibberley, C., &  
 639 Withjack, M. (2010, November). A review of recent developments concern-  
 640 ing the structure, mechanics and fluid flow properties of fault zones. *Jour-*  
 641 *nal of Structural Geology*, 32(11), 1557–1575. Retrieved 2022-01-08, from  
 642 <https://linkinghub.elsevier.com/retrieve/pii/S019181411000101X>  
 643 [doi: 10.1016/j.jsg.2010.06.009](https://linkinghub.elsevier.com/retrieve/pii/S019181411000101X)
- 644 Field, E. H., Arrowsmith, R. J., Biasi, G. P., Bird, P., Dawson, T. E., Felzer, K. R.,  
 645 ... Zeng, Y. (2014, June). Uniform California Earthquake Rupture Forecast,  
 646 Version 3 (UCERF3)–The Time-Independent Model. *Bulletin of the Seismo-*  
 647 *logical Society of America*, 104(3), 1122–1180. Retrieved 2022-01-11, from

- 648 [https://pubs.geoscienceworld.org/bssa/article/104/3/1122-1180/](https://pubs.geoscienceworld.org/bssa/article/104/3/1122-1180/351420)  
 649 351420 doi: 10.1785/0120130164
- 650 Fohrmann, M., Igel, H., Jahnke, G., & Ben-Zion, Y. (2004, December). Guided  
 651 Waves from Sources Outside Faults: An Indication for Shallow Fault Zone  
 652 Structure? *Pure and Applied Geophysics*, 161(11-12). Retrieved 2022-02-  
 653 17, from <http://link.springer.com/10.1007/s00024-004-2553-y> doi:  
 654 10.1007/s00024-004-2553-y
- 655 Freed, A. M., & Lin, J. (2001, May). Delayed triggering of the 1999 Hector Mine  
 656 earthquake by viscoelastic stress transfer. *Nature*, 411(6834), 180–183. Re-  
 657 trieved 2022-06-02, from <http://www.nature.com/articles/35075548> doi:  
 658 10.1038/35075548
- 659 Graves, R. W., & Pitarka, A. (2010, October). Broadband Ground-Motion Sim-  
 660 ulation Using a Hybrid Approach. *Bulletin of the Seismological Society*  
 661 *of America*, 100(5A), 2095–2123. Retrieved 2022-01-11, from [https://](https://pubs.geoscienceworld.org/bssa/article/100/5A/2095-2123/325180)  
 662 [pubs.geoscienceworld.org/bssa/article/100/5A/2095-2123/325180](https://pubs.geoscienceworld.org/bssa/article/100/5A/2095-2123/325180)  
 663 doi: 10.1785/0120100057
- 664 Harris, R. A., & Day, S. M. (1993, March). Dynamics of fault interaction: parallel  
 665 strike-slip faults. *Journal of Geophysical Research: Solid Earth*, 98(B3), 4461–  
 666 4472. Retrieved 2022-01-08, from <http://doi.wiley.com/10.1029/92JB02272>  
 667 doi: 10.1029/92JB02272
- 668 Harris, R. A., & Day, S. M. (1999, July). Dynamic 3D simulations of earthquakes  
 669 on En Echelon Faults. *Geophysical Research Letters*, 26(14), 2089–2092. Re-  
 670 trieved 2022-01-08, from <http://doi.wiley.com/10.1029/1999GL900377> doi:  
 671 10.1029/1999GL900377
- 672 Jousset, P. (2019, November). Illuminating Earth’s faults. *Science*, 366(6469), 1076–  
 673 1077. Retrieved 2022-01-11, from [https://www.science.org/doi/10.1126/](https://www.science.org/doi/10.1126/science.aaz7750)  
 674 [science.aaz7750](https://www.science.org/doi/10.1126/science.aaz7750) doi: 10.1126/science.aaz7750
- 675 Joyce, K. E., Belliss, S. E., Samsonov, S. V., McNeill, S. J., & Glassey, P. J. (2009,  
 676 April). A review of the status of satellite remote sensing and image processing  
 677 techniques for mapping natural hazards and disasters. *Progress in Physical*  
 678 *Geography: Earth and Environment*, 33(2), 183–207. Retrieved 2022-01-11,  
 679 from <http://journals.sagepub.com/doi/10.1177/0309133309339563> doi:  
 680 10.1177/0309133309339563
- 681 Kiser, E., & Ishii, M. (2017, August). Back-Projection Imaging of Earthquakes.  
 682 *Annual Review of Earth and Planetary Sciences*, 45(1), 271–299. Re-  
 683 trieved 2021-05-10, from [http://www.annualreviews.org/doi/10.1146/](http://www.annualreviews.org/doi/10.1146/annurev-earth-063016-015801)  
 684 [annurev-earth-063016-015801](http://www.annualreviews.org/doi/10.1146/annurev-earth-063016-015801) doi: 10.1146/annurev-earth-063016-015801
- 685 Kurzon, I., Vernon, F. L., Ben-Zion, Y., & Atkinson, G. (2014, November).  
 686 Ground Motion Prediction Equations in the San Jacinto Fault Zone: Sig-  
 687 nificant Effects of Rupture Directivity and Fault Zone Amplification. *Pure*  
 688 *and Applied Geophysics*, 171(11), 3045–3081. Retrieved 2022-01-11,  
 689 from <http://link.springer.com/10.1007/s00024-014-0855-2> doi:  
 690 10.1007/s00024-014-0855-2
- 691 Lai, V. H., Graves, R. W., Yu, C., Zhan, Z., & Helmberger, D. V. (2020, October).  
 692 Shallow Basin Structure and Attenuation Are Key to Predicting Long Shaking  
 693 Duration in Los Angeles Basin. *Journal of Geophysical Research: Solid Earth*,  
 694 125(10). Retrieved 2022-02-02, from [https://onlinelibrary.wiley.com/](https://onlinelibrary.wiley.com/doi/10.1029/2020JB019663)  
 695 [doi/10.1029/2020JB019663](https://onlinelibrary.wiley.com/doi/10.1029/2020JB019663) doi: 10.1029/2020JB019663
- 696 Lay, V., Buske, S., Townend, J., Kellett, R., Savage, M., Schmitt, D. R., ... Kof-  
 697 man, R. (2021, December). 3D Active Source Seismic Imaging of the Alpine  
 698 Fault Zone and the Whataroa Glacial Valley in New Zealand. *Journal of*  
 699 *Geophysical Research: Solid Earth*, 126(12). Retrieved 2022-01-11, from  
 700 <https://onlinelibrary.wiley.com/doi/10.1029/2021JB023013> doi:  
 701 10.1029/2021JB023013
- 702 Li, Z., Shen, Z., Yang, Y., Williams, E., Wang, X., & Zhan, Z. (2021, June).

- 703 Rapid Response to the 2019 Ridgecrest Earthquake With Distributed  
 704 Acoustic Sensing. *AGU Advances*, 2(2). Retrieved 2022-02-01, from  
 705 <https://onlinelibrary.wiley.com/doi/10.1029/2021AV000395> doi:  
 706 10.1029/2021AV000395
- 707 Liberty, L. M., St. Clair, J., & McKean, A. P. (2021, April). A Broad, Distributed  
 708 Active Fault Zone Lies beneath Salt Lake City, Utah. *The Seismic Record*,  
 709 1(1), 35–45. Retrieved 2021-11-29, from [https://pubs.geoscienceworld](https://pubs.geoscienceworld.org/tsr/article/1/1/35/600687/A-Broad-Distributed-Active-Fault-Zone-Lies-beneath)  
 710 [.org/tsr/article/1/1/35/600687/A-Broad-Distributed-Active-Fault](https://pubs.geoscienceworld.org/tsr/article/1/1/35/600687/A-Broad-Distributed-Active-Fault-Zone-Lies-beneath)  
 711 [-Zone-Lies-beneath](https://pubs.geoscienceworld.org/tsr/article/1/1/35/600687/A-Broad-Distributed-Active-Fault-Zone-Lies-beneath) doi: 10.1785/0320210009
- 712 Lin, Y.-P., & Jordan, T. H. (2018, July). Frequency-Dependent Attenuation  
 713 of *P* and *S* Waves in Southern California. *Journal of Geophysical Re-*  
 714 *search: Solid Earth*, 123(7), 5814–5830. Retrieved 2022-02-02, from [http://](http://doi.wiley.com/10.1029/2018JB015448)  
 715 [doi.wiley.com/10.1029/2018JB015448](http://doi.wiley.com/10.1029/2018JB015448) doi: 10.1029/2018JB015448
- 716 Lindsey, N. J., Dawe, T. C., & Ajo-Franklin, J. B. (2019, November). Illu-  
 717 minating seafloor faults and ocean dynamics with dark fiber distributed  
 718 acoustic sensing. *Science*, 366(6469), 1103–1107. Retrieved 2022-01-11,  
 719 from <https://www.science.org/doi/10.1126/science.aay5881> doi:  
 720 10.1126/science.aay5881
- 721 Lindsey, N. J., Rademacher, H., & Ajo-Franklin, J. B. (2020, February). On the  
 722 Broadband Instrument Response of Fiber-Optic DAS Arrays. *Journal of Geo-*  
 723 *physical Research: Solid Earth*, 125(2). Retrieved 2022-06-09, from [https://](https://onlinelibrary.wiley.com/doi/abs/10.1029/2019JB018145)  
 724 [onlinelibrary.wiley.com/doi/abs/10.1029/2019JB018145](https://onlinelibrary.wiley.com/doi/abs/10.1029/2019JB018145) doi: 10.1029/  
 725 2019JB018145
- 726 McGuire, J., & Ben-Zion, Y. (2005, October). High-resolution imaging of the  
 727 Bear Valley section of the San Andreas fault at seismogenic depths with fault-  
 728 zone head waves and relocated seismicity. *Geophysical Journal International*,  
 729 163(1), 152–164. Retrieved 2022-01-19, from [https://academic.oup.com/](https://academic.oup.com/gji/article-lookup/doi/10.1111/j.1365-246X.2005.02703.x)  
 730 [gji/article-lookup/doi/10.1111/j.1365-246X.2005.02703.x](https://academic.oup.com/gji/article-lookup/doi/10.1111/j.1365-246X.2005.02703.x) doi:  
 731 10.1111/j.1365-246X.2005.02703.x
- 732 Muir, J. B., & Zhan, Z. (2021, June). Seismic wavefield reconstruction using a  
 733 pre-conditioned wavelet–curvelet compressive sensing approach. *Geophys-*  
 734 *ical Journal International*, 227(1), 303–315. Retrieved 2022-06-09, from  
 735 <https://academic.oup.com/gji/article/227/1/303/6294467> doi:  
 736 10.1093/gji/ggab222
- 737 Qin, L., Share, P.-E., Qiu, H., Allam, A. A., Vernon, F. L., & Ben-Zion, Y. (2020,  
 738 November). Internal structure of the San Jacinto fault zone at the Ramona  
 739 Reservation, north of Anza, California, from dense array seismic data. *Geo-*  
 740 *physical Journal International*, 224(2), 1225–1241. Retrieved 2022-06-01,  
 741 from <https://academic.oup.com/gji/article/224/2/1225/5936338> doi:  
 742 10.1093/gji/ggaa482
- 743 Qiu, H., Ben-Zion, Y., Catchings, R., Goldman, M. R., Allam, A. A., & Steidl,  
 744 J. (2021, July). Seismic Imaging of the Mw 7.1 Ridgecrest Earthquake  
 745 Rupture Zone From Data Recorded by Dense Linear Arrays. *Journal of*  
 746 *Geophysical Research: Solid Earth*, 126(7). Retrieved 2022-02-16, from  
 747 <https://onlinelibrary.wiley.com/doi/10.1029/2021JB022043> doi:  
 748 10.1029/2021JB022043
- 749 Ross, Z. E., Idini, B., Jia, Z., Stephenson, O. L., Zhong, M., Wang, X., ... Jung,  
 750 J. (2019, October). Hierarchical interlocked orthogonal faulting in the 2019  
 751 Ridgecrest earthquake sequence. *Science*, 366(6463), 346–351. Retrieved 2021-  
 752 11-09, from <https://www.science.org/doi/10.1126/science.aaz0109> doi:  
 753 10.1126/science.aaz0109
- 754 Scholtz, C. (2019). *The Mechanics of Earthquakes and Faulting*. Cambridge, U.K.:  
 755 Cambridge University Press.
- 756 Share, P. E., & Ben-Zion, Y. (2018, November). A Bimaterial Interface Along  
 757 the Northern San Jacinto Fault Through Cajon Pass. *Geophysical Research*

- 758 *Letters*, 45(21). Retrieved 2022-06-01, from [https://onlinelibrary.wiley](https://onlinelibrary.wiley.com/doi/10.1029/2018GL079834)  
 759 [.com/doi/10.1029/2018GL079834](https://onlinelibrary.wiley.com/doi/10.1029/2018GL079834) doi: 10.1029/2018GL079834
- 760 Share, P. E., Qiu, H., Vernon, F. L., Allam, A. A., Fialko, Y., & Ben-Zion, Y.  
 761 (2022, January). General Seismic Architecture of the Southern San An-  
 762 dreas Fault Zone around the Thousand Palms Oasis from a Large-N Nodal  
 763 Array. *The Seismic Record*, 2(1), 50–58. Retrieved 2022-06-01, from  
 764 [https://pubs.geoscienceworld.org/tsr/article/2/1/50/612139/General](https://pubs.geoscienceworld.org/tsr/article/2/1/50/612139/General-Seismic-Architecture-of-the-Southern-San)  
 765 [-Seismic-Architecture-of-the-Southern-San](https://pubs.geoscienceworld.org/tsr/article/2/1/50/612139/General-Seismic-Architecture-of-the-Southern-San) doi: 10.1785/0320210040
- 766 Share, P.-E., Tábořík, P., Štěpančíková, P., Stemberk, J., Rockwell, T. K., Wade,  
 767 A., ... Ben-Zion, Y. (2020, August). Characterizing the uppermost 100 m  
 768 structure of the San Jacinto fault zone southeast of Anza, California, through  
 769 joint analysis of geological, topographic, seismic and resistivity data. *Geo-*  
 770 *physical Journal International*, 222(2), 781–794. Retrieved 2022-06-20,  
 771 from <https://academic.oup.com/gji/article/222/2/781/5834548> doi:  
 772 10.1093/gji/ggaa204
- 773 Small, P., Gill, D., Maechling, P. J., Taborda, R., Callaghan, S., Jordan, T. H., ...  
 774 Goulet, C. (2017, November). The SCEC Unified Community Velocity Model  
 775 Software Framework. *Seismological Research Letters*, 88(6), 1539–1552. Re-  
 776 trieved 2021-12-10, from [https://pubs.geoscienceworld.org/srl/article/](https://pubs.geoscienceworld.org/srl/article/88/6/1539-1552/353986)  
 777 [88/6/1539-1552/353986](https://pubs.geoscienceworld.org/srl/article/88/6/1539-1552/353986) doi: 10.1785/0220170082
- 778 Song, J., & Yang, H. (2022, January). Seismic Site Response Inferred From Records  
 779 at a Dense Linear Array Across the Chenghai Fault Zone, Binchuan, Yunnan.  
 780 *Journal of Geophysical Research: Solid Earth*, 127(1). Retrieved 2022-06-01,  
 781 from <https://onlinelibrary.wiley.com/doi/10.1029/2021JB022710> doi:  
 782 10.1029/2021JB022710
- 783 Spica, Z. J., Castellanos, J. C., Viens, L., Nishida, K., Akuhara, T., Shino-  
 784 hara, M., & Yamada, T. (2022, January). Subsurface Imaging With  
 785 Ocean-Bottom Distributed Acoustic Sensing and Water Phases Reverber-  
 786 ations. *Geophysical Research Letters*, 49(2). Retrieved 2022-06-02, from  
 787 <https://onlinelibrary.wiley.com/doi/10.1029/2021GL095287> doi:  
 788 10.1029/2021GL095287
- 789 Spica, Z. J., Nishida, K., Akuhara, T., Pétrélis, F., Shinohara, M., & Yamada, T.  
 790 (2020, August). Marine Sediment Characterized by Ocean-Bottom Fiber-Optic  
 791 Seismology. *Geophysical Research Letters*, 47(16). Retrieved 2022-01-11,  
 792 from <https://onlinelibrary.wiley.com/doi/10.1029/2020GL088360> doi:  
 793 10.1029/2020GL088360
- 794 Thakur, P., Huang, Y., & Kaneko, Y. (2020, August). Effects of Low-Velocity Fault  
 795 Damage Zones on Long-Term Earthquake Behaviors on Mature Strike-Slip  
 796 Faults. *Journal of Geophysical Research: Solid Earth*, 125(8). Retrieved 2022-  
 797 01-14, from <https://onlinelibrary.wiley.com/doi/10.1029/2020JB019587>  
 798 doi: 10.1029/2020JB019587
- 799 USGS, & CGS. (2022). *Quaternary fault and fold database for the united states*.  
 800 Retrieved from <https://www.usgs.gov/natural-hazards/earthquake>  
 801 [-hazards/faults](https://www.usgs.gov/natural-hazards/earthquake-hazards/faults)
- 802 Wang, H. F., Zeng, X., Miller, D. E., Fratta, D., Feigl, K. L., Thurber, C. H., &  
 803 Mellors, R. J. (2018, June). Ground motion response to an ML 4.3 earth-  
 804 quake using co-located distributed acoustic sensing and seismometer arrays.  
 805 *Geophysical Journal International*, 213(3), 2020–2036. Retrieved 2022-06-09,  
 806 from <https://academic.oup.com/gji/article/213/3/2020/4942237> doi:  
 807 10.1093/gji/ggy102
- 808 Wang, Y., Allam, A., & Lin, F. (2019, November). Imaging the Fault Damage Zone  
 809 of the San Jacinto Fault Near Anza With Ambient Noise Tomography Using a  
 810 Dense Nodal Array. *Geophysical Research Letters*, 46(22), 12938–12948. Re-  
 811 trieved 2022-06-20, from [https://onlinelibrary.wiley.com/doi/10.1029/](https://onlinelibrary.wiley.com/doi/10.1029/2019GL084835)  
 812 [2019GL084835](https://onlinelibrary.wiley.com/doi/10.1029/2019GL084835) doi: 10.1029/2019GL084835

- 813 Weng, H., Yang, H., Zhang, Z., & Chen, X. (2016, June). Earthquake rupture  
 814 extents and coseismic slips promoted by damaged fault zones: Ruptures Pro-  
 815 moted by Fault Zones. *Journal of Geophysical Research: Solid Earth*, *121*(6),  
 816 4446–4457. Retrieved 2022-01-08, from [http://doi.wiley.com/10.1002/](http://doi.wiley.com/10.1002/2015JB012713)  
 817 [2015JB012713](http://doi.wiley.com/10.1002/2015JB012713) doi: 10.1002/2015JB012713
- 818 Wesnousky, S. G. (2008, August). Displacement and Geometrical Characteristics  
 819 of Earthquake Surface Ruptures: Issues and Implications for Seismic-Hazard  
 820 Analysis and the Process of Earthquake Rupture. *Bulletin of the Seismological*  
 821 *Society of America*, *98*(4), 1609–1632. Retrieved 2022-01-10, from [https://](https://pubs.geoscienceworld.org/bssa/article/98/4/1609-1632/350111)  
 822 [pubs.geoscienceworld.org/bssa/article/98/4/1609-1632/350111](https://pubs.geoscienceworld.org/bssa/article/98/4/1609-1632/350111) doi:  
 823 10.1785/0120070111
- 824 Wessel, P., Luis, J. F., Uieda, L., Scharroo, R., Wobbe, F., Smith, W. H. F., &  
 825 Tian, D. (2019). *The generic mapping tools*. Retrieved from [https://](https://www.generic-mapping-tools.org/)  
 826 [www.generic-mapping-tools.org/](https://www.generic-mapping-tools.org/)
- 827 Xu, X., Sandwell, D. T., & Smith-Konter, B. (2020, July). Coseismic Displacements  
 828 and Surface Fractures from Sentinel-1 InSAR: 2019 Ridgecrest Earthquakes.  
 829 *Seismological Research Letters*, *91*(4), 1979–1985. Retrieved 2021-11-09,  
 830 from [https://pubs.geoscienceworld.org/ssa/srl/article/91/4/1979/](https://pubs.geoscienceworld.org/ssa/srl/article/91/4/1979/580045/Coseismic-Displacements-and-Surface-Fractures-from)  
 831 [580045/Coseismic-Displacements-and-Surface-Fractures-from](https://pubs.geoscienceworld.org/ssa/srl/article/91/4/1979/580045/Coseismic-Displacements-and-Surface-Fractures-from) doi:  
 832 10.1785/0220190275
- 833 Yang, H., Duan, Y., Song, J., Jiang, X., Tian, X., Yang, W., ... Yang, J. (2020,  
 834 July). Fine Structure of the Chenghai Fault Zone, Yunnan, China, Constrained  
 835 From Teleseismic Travel Time and Ambient Noise Tomography. *Journal*  
 836 *of Geophysical Research: Solid Earth*, *125*(7). Retrieved 2022-06-01, from  
 837 <https://onlinelibrary.wiley.com/doi/10.1029/2020JB019565> doi:  
 838 10.1029/2020JB019565
- 839 Yang, Y., Atterholt, J. W., Shen, Z., Muir, J. B., Williams, E. F., & Zhan,  
 840 Z. (2022, January). Sub-Kilometer Correlation Between Near-Surface  
 841 Structure and Ground Motion Measured With Distributed Acoustic Sens-  
 842 ing. *Geophysical Research Letters*, *49*(1). Retrieved 2022-01-11, from  
 843 <https://onlinelibrary.wiley.com/doi/10.1029/2021GL096503> doi:  
 844 10.1029/2021GL096503
- 845 Yang, Y., Zhan, Z., Shen, Z., & Atterholt, J. (2022). Fault zone imaging with dis-  
 846 tributed acoustic sensing: Surface-wave scattering.
- 847 Zigone, D., Ben-Zion, Y., Lehujeur, M., Campillo, M., Hillers, G., & Vernon,  
 848 F. L. (2019, May). Imaging subsurface structures in the San Jacinto fault  
 849 zone with high-frequency noise recorded by dense linear arrays. *Geophys-*  
 850 *ical Journal International*, *217*(2), 879–893. Retrieved 2022-06-20, from  
 851 <https://academic.oup.com/gji/article/217/2/879/5305860> doi:  
 852 10.1093/gji/ggz069